International Journal of Mechanical Design and Materials Science
Volume 1, Issue 3 2025

Combined Level-Set-XFEM-Density Topology Optimization for Large Deformation in 4D Printed Structures

Jun Lv , Zheng. Department of Mechanics, Italy

Research Article

Date of Submission: 10-05-2025 **Date of Acceptance: 19-06-2025** **Date of Publication: 1-07-2025**

ABSTRACT

Design tools that take advantage of the growing fabrication flexibility are becoming more and more necessary as additive manufacturing advances. With a precision of tens of microns, multi-material 3D printing enables the creation of components from several materials with distinct mechanical, thermal, and "active" behaviors that may be organized spatially in three dimensions. Shape-changing characteristics may be included into additively built structures by taking advantage of this. 4D printing is 3D printing that changes its form downstream in reaction to an environmental input like light, humidity, or temperature. In order to produce active structures that experience significant deformation and assume a desirable target displacement upon heat activation, a design technique for determining the material layout of 4D printed materials with internal, programmable stresses is presented in this study. The dynamic multi-material design issue is described in the optimization process by combining density-based topology optimization with a level set approach and the extended finite element method (XFEM). To precisely forecast the behavior of nonlinear slender structures throughout the design development, a higher-order XFEM method is combined with a finite deformation hyperelastic thermomechanical model. The special capabilities of the suggested framework are shown using examples. When 4D printed physical specimens and numerical predictions of optimum shape-changing structures are compared, excellent agreement is found. All things considered, a methodical design strategy that produces non-intuitive material layouts and geometries to accomplish goal deformations of varying complexity is described for the creation of 4D printed active structures with geometrically nonlinear behavior.

Introduction

The precision, material diversity, and dependability of advanced additive manufacturing (AM) technologies, such as three-dimensional (3D) printing, have significantly increased in recent years. The idea of 4D printing, which uses external inputs to cause form changes after a building is 3D printed, was recently presented by [1]. Thus, the fourth dimension is the shape-change throughout time. Using the thermomechanical reaction of a glassy polymer within an elastomer matrix, this idea was used in [2] to create morphing shape memory polymer structures. In order to produce active origami structures, a comparable material response was investigated in [3]. [4] employed level set (LS) topology optimization to produce printed active composites that take on a desired form after a thermomechanical training and activation cycle by taking use of the shape memory ability of a 3D printed glassy polymer. According to [5], the disadvantage of these conventional 4D printing methods is the need for a complicated thermomechanical training and activation cycle in order to initiate a shape-change. In order to address this problem, [5] presented a revolutionary method known as "direct 4D printing," in which the form change happens while printing without the need for an external training cycle. An inelastic eigenstrain that is encoded into the 3D printed structure during the printing process is known as the "printing strain," and it is employed in this way to create a form change. By adjusting the duration and intensity of the UV-curing of photopolymers during the polyjet process, the compressive strain's magnitude may be controlled. In this study, a desired shape change upon release of the built-in eigenstrain is achieved by using two polymers with distinct eigenstrain magnitudes and glass transition temperatures. Therefore, a component made in this way is made up of many well-bonded polymers with a high-fidelity geometry, each of which has an eigenstrain that varies spatially. After printing, the component is heated to reduce the stiffness of the glassy polymer (passive material) and unleash the inherent eigenstrain of the rubbery polymer (active material). This is accomplished by heating the printed structure over the passive material's glass transition temperature, which permanently alters its form. As an alternative, [6] and [7] have suggested a frontal polymerization process. This method produces 4D printed self-folding origami structures by using the variation in light polymerization intensity to generate spatially changing material characteristics. A solvent entering a loose polymer matrix generates isotropic swelling, which in turn causes shape alterations. In this study, spatially variable eigenstrains are conveniently included during the production of self-actuating plate-like structures using the direct 4D printing approach. The interested reader is directed to [5] for a more

thorough examination of the direct 4D printing technique. An inverse design problem is stated and addressed to take advantage of spatially variable inelastic stresses to achieve complicated target displacements upon activation. The ideal shape and material arrangement of active 4D printed components are systematically established given a specified goal deformation. This has only been done for 1D rod constructions or basic target shapes [5] in earlier studies [8] and [9], when it was feasible to predict the ideal material architecture in advance. instinctively. For self-folding composite structures, a comparable method based on traditional origami patterns is shown in [10]. The material arrangement of shape-changing 4D printed objects enduring significant deformation is determined in this research using a novel multi-material topology optimization technique. The suggested computational design approach uses a higher-order extended finite element method (XFEM) formulation in conjunction with a hyperelastic thermomechanical model to accurately represent the physical response of the structure. The multi-material design challenge is solved via a hybrid method that combines density-based topology optimization with LS-XFEM. Each of these topology optimization techniques has shown to have a broad variety of applications. LS and density topology optimization techniques are summarized in [11], [12], and [13], respectively. The topic of design optimization of self-folding structures is another area where topology optimization is applied. For instance, [14] used a density-based approach to improve the arrangement of monolithic liquid crystal elastomers in order to produce folding liquid crystal elastomer actuators. Nevertheless, the precision of this method is severely limited by a simplified linear elastic model working in the small strain region. In order to create active 3D origami and kirigami structures utilizing 4D printing, [15] used a more simpler method that uses shape optimization to get the best cut plan. Additionally, [16] recently used a genetic algorithm (GA) in conjunction with the idea of moveable morphable components (MMC) [17] to optimize the topology of post-buckled 3D kirigami constructions. Only a subset of all potential designs is investigated, despite the fact that each of these methods significantly lowers the number of design variables and, thus, the complexity of the optimization issue. This research proposes a combined LS-XFEM and density topology optimization approach for building 4D printed active structures that takes into account a completely nonlinear structural response while using the whole design space. Target displacement matching is the goal, and Fig. 1 conceptually depicts the design, production, and activation process of 4D printed structures as suggested in this study. This may be accomplished by either defining the needed displacement of specific points of the structure in order to produce the desired deformation, or by defining the intended target shape, which is the location of points of the structure in the deformed (activated) configuration. In this study, target deformations are achieved by specifying the target displacement of target points on the domain border (Fig. 1 (a)). An initial arrangement of solid and void domains is defined using a level set function (LSF) starting with an initially flat plate (b). The various characteristics of an active and a passive material are interpolated within the solid domain using a fictional density field. On the XFEM backdrop mesh, the density distributions and the LSF are both discretized. A nonlinear programming approach is then used to address the ensuing parameter optimization issue. Sub-domains of active and passive material are retrieved in a post-processing phase (d) after the discovery of a final design (i.e., geometry and material distribution) (c). After the flat framework has been

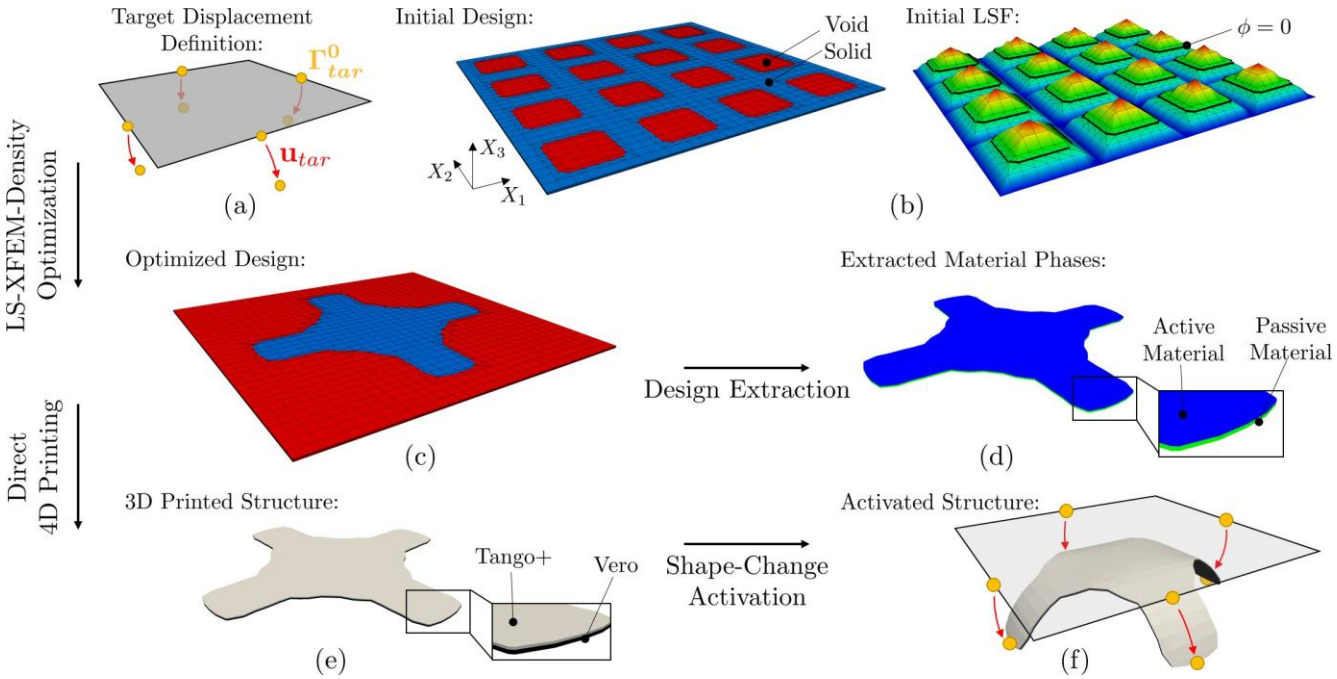


Fig. 1. Conceptual steps of the design process from (a) the definition of a target displacement to (f) an activated structure using direct 4D printing.

printed (e), the shape-change is activated through relaxation of the compressive printing strain in the active material in a 65.0°C hot water bath. This is achieved by heating up the structure above the glass transition temperature of the passive, stiff material at which its stiffness is significantly reduced. At this state, the eigenstrains of the active material can relax leading to the desired change in shape. After a subsequent cool-down, the passive material stiffens and a permanently deformed structure is obtained (f).

The theoretical background of the physical model, the spatial discretization of state and optimization variables, and the optimization problem along with examples are presented in the remainder of this paper, which is organized as follows: Sec. 2 introduces the continuum model of the nonlinear thermomechanical phenomena. Sec. 3 provides details on the optimization approach and the XFEM model. Sec. 4 describes the validation of the thermomechanical model, and design optimization examples are presented in Sec. 5 along with experimental results. A summary of the work is presented in Sec. 6.

Hyperelastic Thermomechanical Model

The total design domain Ω^0 is comprised of solid and void sub-domains (i.e. Ω^0 and Ω^0), such that $\Omega^0 = \Omega^0 \cup \Omega^0$.

D S V D S V

Within the solid domain

Ω^0

S (see Fig. 2 (a)), balance of linear momentum in the undeformed configuration is described by the static equilibrium. The weak form of the governing equation using a total Lagrangian formulation is stated as:

$$\mathbf{R} = \int_{\Omega_S} (\delta\mathbf{F} : \mathbf{P} - \delta\mathbf{u}\,\rho_0\mathbf{B})\,dV - \int_{\Gamma_T^-} \delta\mathbf{u}\,\bar{\mathbf{T}}\;dA = 0 \quad (1)$$

where $\mathbf{F} = \partial\mathbf{x}/\partial\mathbf{X}$ is the total deformation gradient tensor with $\mathbf{x} = \mathbf{u} + \mathbf{X}$ defining the relation between spatial coordinates in the undeformed ($\mathbf{X}$) and deformed ($\mathbf{x}$) configurations Ω^0 and Ω_S respectively. The displacements are denoted by $\mathbf{u}$ and $\delta\mathbf{u}$ are the admissible test functions. The first Piola-Kirchhoff stress tensor is denoted by $\mathbf{P}$ and $\mathbf{B}$ is the prescribed body force vector in the undeformed configuration. The density is denoted by ρ_0 and $\bar{\mathbf{u}}$ is the prescribed displacement field on Γ^0, see Fig. 2 (a). The prescribed traction vector on Γ^0 is $\bar{\mathbf{T}}$ and the total design domain boundary Γ^0 is comprised of $\Gamma^0 = \Gamma_{\bar{u}}^0 \cup \Gamma_{\bar{T}}^0$. A hyperelastic Saint Venant-Kirchhoff constitutive model for isotropic compressible solids is used in the current work. The hyperelastic Saint Venant-Kirchhoff material model is suitable for large deformations at small strains, which is the case for the slender structures targeted in this work. The proposed design optimization framework can easily be extended to operate on nonlinear constitutive models for both compressible and incompressible materials. This is especially

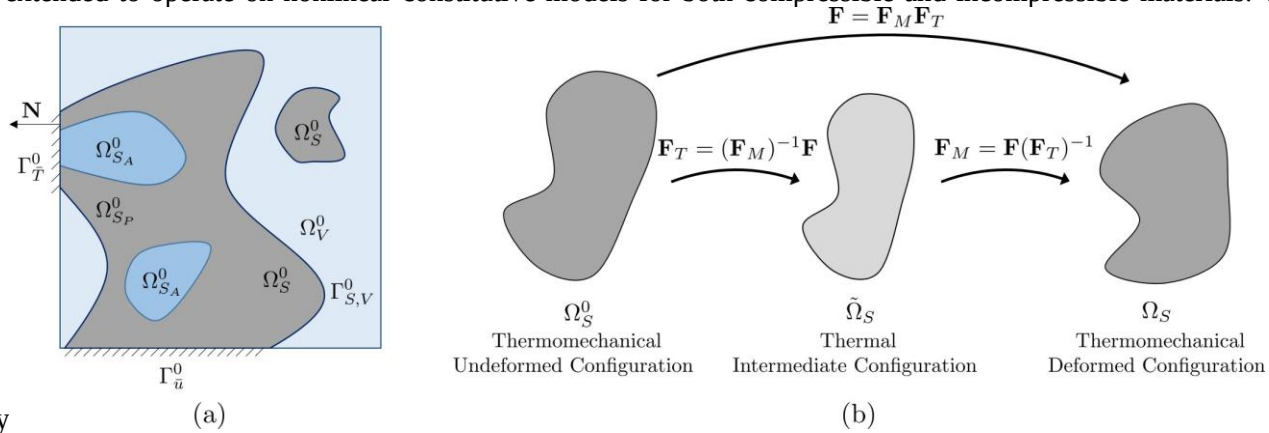


Fig. 2. (a) Design domain decomposition into solid (Ω^0) and void (Ω^0) sub-domains using LS-XFEM along the interface Γ^0. Within the solid domain, a further distinction is made between an active material (Ω^0) and a passive material (Ω^0). (b) Multiplicative decomposition of the total deformation gradient into thermal and mechanical deformation gradient.

relevant for simulating rubbery, nearly-incompressible polymers and therefore should be treated in future work. The Saint Venant-Kirchhoff material model is defined as:

$$\tilde{\mathbf{S}} = 2\mu\,\mathbf{E}_M + \lambda\,\mathrm{tr}(\mathbf{E}_M)\mathbf{I} \quad (2)$$

where $\tilde{\mathbf{S}}$ is the second Piola-Kirchhoff stress tensor in the intermediate configuration (see Fig. 2 (b)) and $\mathbf{E}_M$ is the Green-Lagrange strain tensor defined as the deformation of the intermediate configuration to the thermomechanical deformed configuration. The second order identity tensor is denoted by **I**. The Lame´ constants are denoted by μ and λ which are related to the Young's modulus E and Poisson's ratio ν as follows:

(3)

In the context of topology optimization using the density method, the Young's modulus is manipulated as a function of the design variables whereas the Poisson's ratio is kept constant. A more detailed discussion of the optimization problem is presented in Sec. 3.1.

To model the inelastic printing strain built into the elastomer, a residual thermal strain model is used as suggested by [5]. In a finite deformation case, special consideration with respect to the decomposition of the total deformation gradient is required. As indicated in Fig. 2 (b), a multiplicative decomposition of the total deformation gradient $\mathbf{F}$ into an inelastic thermal deformation gradient $\mathbf{F}_T$ and an elastic mechanical deformation gradient $\mathbf{F}_M$ is used. The multiplicative decomposition of the total deformation gradient can be stated as:

$$\mathbf{F} = \mathbf{F}_M \mathbf{F}_T \quad (4)$$

For the thermal deformation gradient tensor, a linear thermal expansion model is assumed:

$$\mathbf{F}_T = (1 + \alpha_k [\bar{T} - T_0])\mathbf{I} \quad (5)$$

where α_k is the linear coefficient of thermal expansion (CTE) of either solid material (k = active or passive) representing the amount of inelastic expansion. The externally applied temperature is $\bar{T}$ which is a linear function of pseudo time of the
deformation process and T_0 is the reference temperature. Using the previously defined relationships, the Green-Lagrange strain tensor is defined as:

$$\mathbf{E}_M = \frac{1}{2}(\mathbf{C}_M - \mathbf{I}) \quad (6)$$

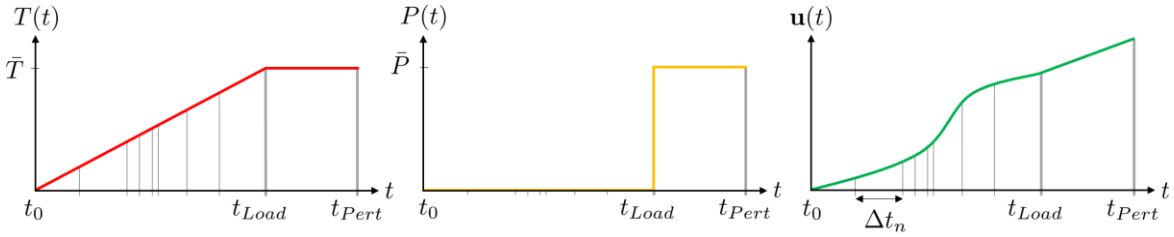


Fig. 3. Adaptive load-stepping technique used to solve the nonlinear problem. (a) Temperature load profile, (b) follower load profile and (c) displacement response over pseudo time.

where the right Cauchy-Green deformation tensor is $\mathbf{C}_M = (\mathbf{F}_M)^T \mathbf{F}_M$.

For integration of the governing equation stated in Eqn. (1) in the undeformed configuration, the second Piola-Kirchhoff stress tensor $\tilde{\mathbf{S}}$ is pulled-back from the intermediate configuration $\tilde{\Omega}_S$ to the undeformed configuration ${}^{S}\Omega^{0}$ using the Piola-transform. This transformation is defined as:

$$\mathbf{S} = (\mathbf{F}_T)^{-1} \tilde{\mathbf{S}} (\mathbf{F}_T)^{-T} J_T \quad (7)$$

where J_T is the Jacobian of the thermal deformation gradient tensor $J_T = \det(\mathbf{F}_T)$. The first Piola-Kirchhoff stress tensor in the undeformed configuration is finally computed as:

$$\mathbf{P} = \mathbf{F}\,\mathbf{S} \quad (8)$$

Follower Pressure Load

In order to enforce an end-stiffness constraint on the final, deformed structure, a follower pressure load is introduced and added to the weak form of the governing equation (1). To this end, a deformation dependent (i.e. follower)

Neumann boundary condition is employed, which is formulated in the deformed configuration and mapped back to the undeformed configuration. Using Nanson's formula [18], the relationship between surface areas in the undeformed and deformed con-figuration is defined. The non-conservative follower pressure can simply be evaluated in the undeformed configuration as follows:

$$\mathbf{R}_{\Gamma P} = -\int_{\Gamma^0} \delta\mathbf{u}\,(\mathbf{F})^{-T}\,\mathbf{N}\,J\,\bar{P}\,dA \quad (9)$$
$$\bar{T}$$

where dA is an infinitesimal surface area in the undeformed configuration, $J = \det(\mathbf{F})$ is the determinant of the total defor-mation gradient and $\mathbf{N}$ is the surface normal in the undeformed configuration. The surface pressure scalar reformulated in the undeformed configuration is denoted by $\bar{P}$. For simplicity it is assumed that $\bar{P}$ is not state dependent. A more detailed discussion of the end-stiffness constraint is presented in Sec. 3.4.

Adaptive Load-Stepping Approach

An adaptive load-stepping approach is used for the XFEM analysis in order to effectively anticipate the nonlinear deformation of 4D printed self-deforming structures. Figure 3 shows the schematic development of the temperature load T (t), applied follower load P(t), and displacement response u(t) as a function of pseudo time t. In the event that a Newton-Raphson solve fails to converge to an equilibrium solution for a predetermined maximum number of nonlinear iterations, an adaptive time-stepping strategy is used to lower the previously selected time step size Δt0 by a factor f. This occurs, for instance, when the structural reaction during the topology optimization process is dominated by domains of intermediate (weak) material. In this case, the time step is adaptively decreased until the lowered time step yields a certain number of (converged) nonlinear solutions. The initial time step size is then progressively restored. To arrive at the final loading time tLoad, the total number of time steps is modified appropriately. To get a maximum value Tα, the temperature load T is raised linearly between t0 and tLoad while the follower surface pressure load P is zero. Figures 3 (a) and (b) illustrate this conceptually. The inelastic printing strain is represented by the greatest value of T¹. A steady non-zero follower perturbation load P∗ is delivered between tLoad and tPert, while the external temperature load is maintained at T¹. For the nonlinear solution to converge quickly—ideally in a single iteration—the size of the non-zero follower perturbation load must be sufficiently minimal. This is true for imposing an end-stiffness restriction that uses a linear notion to measure the change in total strain energy.

Multi-Material Topology Optimization

A multi-material topology optimization approach is adopted to determine the geometry and the spatial material arrange-ment of 4D printed active structures. This approach builds on a LS-XFEM optimization framework previously used to study problems in structural mechanics [4, 19, 20] and fluid mechanics [21, 22]. This section provides an overview of the multi-material topology optimization approach, while more details regarding immersed boundary techniques used for design optimization are provided in [23].

Combined LS-Density Geometry and Material Description

The three-material problem depicted in Fig. 2 (a) is described by a combined LS-density approach. A nodally discretized LSF is used to distinguish between a solid and a void domain where negative LS values ($\varphi_i < 0$) represent the solid domain Ω^0 and positive LS values ($\varphi_i > 0$) represent the void domain Ω^0 . The zero LS iso-contour ($\varphi_i = 0$) represents the phase

$$S \quad V$$
$$0$$

boundary $\Gamma_{S,V}$ between the solid and the void domain. Nodal LS values φ_i are explicitly defined in terms of nodal design variables s^{φ} using a linear filtering scheme as proposed by [24]. This linear filtering technique enhances convergence of the optimization problem by increasing the zone of influence of each design variable and is formulated as:

$$\varphi_i = \frac{\sum_{j=1}^{Nn} w_{ij} s^{\varphi}_j}{\sum_{j=1}^{Nn} w_{ij}}, \qquad w_{ij} = \max(0, r_s - |\mathbf{X}_i - \mathbf{X}_j|) \qquad (10)$$

where N_n is the number of finite element (FE) nodes within the smoothing radius, r_s, and $|\mathbf{X}_i - \mathbf{X}_j|$ is the Euclidean distance between node i and j measured in the undeformed configuration (indicated by a superscript ^{0}). Index i denotes the current node for which the LS value is computed and index j denotes each node within the smoothing radius contributing to the LS value φ_i.

Combining the level set method (LSM) with the XFEM, yields a crisp solid-void interface which is naturally suited for AM reducing the need for post-processing. However, as mentioned in [24] and [12], a strong influence of the final solution on the initial guess is observed in LS-XFEM topology optimization. Moreover, since LS-XFEM topology optimization is solely driven by localized sensitivities along the interface, the appearance of new holes within the solid domain is not possible [4]. One way to mitigate this issue and the dependency of the final design on the initial guess is to use topological derivatives, as suggested by [25]. In the current work, a sufficiently large number of initial void inclusions is used to mitigate this dependency.

In addition, a density-based topology optimization approach is used within the solid domain Ω^0_S in order to distinguish between an active material (Ω^0_{SA}) and a passive material (Ω^0_{SP}). This combined approach allows for the description of the multi-material topology optimization problem at hand. Nodally discretized, fictitious density design variables $0 \leq s^{\tilde{\rho}}_i \leq 1$ are used to track the material distribution within the solid phase. A standard solid isotropic material with penalization (SIMP) approach [26] is adopted. Considering an element-wise constant density interpolation, the material property within an element is defined as:

$$p^e_i(\hat{\rho}^e) = p^e_{min} + (p^e_{max} - p^e_{min})(\hat{\rho}^e)^{\beta} \qquad (11)$$

where p^e represents any elemental material property like the Young's modulus, density or CTE. Physical properties corresponding to the active material and passive material are denoted by p^e_{min} and p^e_{max}, respectively and β is the so called SIMP exponent used to achieve different interpolation behavior. Different SIMP exponents are used for interpolation of different material properties. Elementally averaged fictitious density values $\tilde{\rho}^e$ are obtained from nodal fictitious density design variables $s^{\tilde{\rho}}_i$ as:

$$\tilde{\rho}^e = \frac{N^e_{n_1} \sum_j s^{\tilde{\rho}}_{ij}}{N^e_n} \qquad (12)$$

where N^e is the number of nodes per element j. A linear elemental filter similar to the one stated in Eqn. (10) is then used to compute a smoothed fictitious elemental density $\bar{\rho}^e$ from the elementally averaged fictitious densities $\tilde{\rho}^e$. In addition, a

i j

smoothed Heaviside projection scheme proposed by [27] is used subsequently to mitigate the blurriness introduced by the linear filtering scheme. The projection function used to compute the fictitious projected elemental density $\hat{\rho}^e$ is stated as:

$$\hat{\rho}^e = \frac{\tanh(\gamma(\bar{\rho}^e - \eta)) + \tanh(\gamma \eta)}{\tanh(\gamma(1-\eta)) + \tanh(\gamma \eta)} \quad (13)$$

where γ is the projection sharpness parameter and η is the projection threshold parameter. The projection (13) is applied through a continuation approach where the projection threshold parameter is gradually increased in the optimization process. More details regarding this approach are found in the discussion of the results in Sec. 5.

XFEM Model

The XFEM is used in this work to discretize the weak form of the governing equation (1) on non-conforming sub-domains. This immersed boundary method is utilized to distinguish between the solid (Ω^0) and the void (Ω^0) sub-domains

$S \quad V$

along the interface (Γ^0

$_{S,V}$) defined by the zero LS iso-contour as depicted in Fig. 2 (a). The advantage of this discretization method is that a high spatial resolution of the interface described by the LSM is retained throughout the optimization process while operating on a fixed background mesh, thus avoiding the need for re-meshing. The XFEM approach, however, requires enriching the classical FE approximation spaces with additional shape functions [28] in order to avoid spurious coupling and load transfer between physically disconnected domains. Note that, in general, enrichment functions are also needed to capture weak and strong discontinuities across material phases. However, this requirement does not apply here, as the XFEM is applied to distinguish only between the solid (Ω^0) and the void (Ω^0) phase. Thus, the displacement field only exists

$S \quad V$

within the solid sub-domain and any element within the void phase can be omitted. A generalized Heaviside enrichment approach [29] is used where the displacements in the solid phase are approximated by standard FE shape functions. The nodal displacements $\mathbf{u}_i(\mathbf{X})$ of node i within the solid domain Ω^0 are approximated as [22]:

$$\mathbf{u}_i(\mathbf{X}) = \sum_{m=1}^{M} H(-\varphi(\mathbf{X})) \sum_{k=1}^{N^e} N_k(\mathbf{X}) \delta^{k\,k} \; {}_{mq}\mathbf{u}_{im} \tag{14}$$

where H is the Heaviside function as a function of the LS value $\varphi(\mathbf{X})$ defined as:

$$H(\varphi) = \begin{cases} 1 & \text{if } \varphi(\mathbf{X}) > 0 \\ 0 & \text{if } \varphi(\mathbf{X}) \leq 0 \end{cases} \tag{15}$$

The maximum number of enrichment levels is denoted by M, $N_k(\mathbf{X})$ is the elemental shape function and δ^k is the Kronecker delta which selects the active enrichment level q for node k. δ^k ensures that displacements at node k are only interpolated by a single set of degrees of freedom (DOFs) defined at node position $\mathbf{X}$ such that the partition of unity principle is satisfied [20]. The Heaviside function H is used to only activate shape functions within the solid phase as displacement solutions in the void domain would be physically meaningless. For more details about the generalized Heaviside enrichment strategy employed in this work, the interested reader is referred to [23], [30], and [31].

For stabilization of the XFEM discretization, a geometric preconditioning scheme as proposed by [32] is used. This geometric preconditioner ensures that DOFs with vanishing zones of influence, which arise when the LS intersection is too close to a FE node, are re-scaled or eliminated in order to provide numerical stability.

Dirichlet boundary conditions applied to the solid sub-domain Ω^0 are enforced weakly using Nitsche's method [33]. The
S_D
weak form of the governing equation (1) is augmented with the weak boundary condition residual contribution $\mathbf{R}_\Gamma$ stated as:

$$\mathbf{R}^D = -\int_{\Gamma^0} [[\delta\mathbf{u}]]\,\mathbf{P}(\mathbf{u})\,\mathbf{N}\,dA - \int_{\Gamma^0} \mathbf{P}(\delta\mathbf{u})\,\mathbf{N}\,[[\mathbf{u}]]\,dA + \gamma_D \int_{\Gamma^0} [[\delta\mathbf{u}]]\,[[\mathbf{u}]]\,dA \tag{16}$$

where the jump operator $[[\bullet]]$ is defined as:

$$[[\mathbf{u}]] = \mathbf{u} - \bar{\mathbf{u}}, \quad [[\delta\mathbf{u}]] = \delta\mathbf{u} - \delta\bar{\mathbf{u}} \tag{17}$$

The penalty factor to enforce the prescribed Dirichlet boundary condition $\bar{\mathbf{u}}$ is denoted by γ_D. The first term in Eqn. (16) corresponds to the standard consistency term, the second term to the adjoint consistency, and the last term is the Nitsche penalty term which explicitly controls the accuracy at which the Dirichlet boundary condition is enforced.

Selective Structural Springs

To avoid ill-conditioning of the linear system due to rigid body modes (RBM) of disconnected solid sub-domains surrounded by the void phase (see Fig. 2 (a)), selective structural springs are introduced. This approach was initially proposed by [21] for fluid problems and is extended to nonlinear structural mechanics in this work. To identify disconnected solid domains "floating" within the void domain, an auxiliary indicator field modeled as a linear diffusion problem is introduced within the solid domain. Alternatively, globally applied structural springs could be used, as done by [19]. The weak form of the governing equation for the auxiliary scalar indicator field $\tilde{\theta}$ is formulated as:

$$\mathbf{R}_{Aux} = \int_{\Omega_S} \delta\nabla\tilde{\theta}\,(\kappa\nabla\tilde{\theta}) + \delta\tilde{\theta}\,h(\tilde{\theta} - \tilde{\theta}_{ref})\,dV \qquad (18)$$

where $\delta\tilde{\theta}$ are the admissible test functions and κ denotes the thermal conductivity. The bulk heat transfer coefficient is denoted by h and $\tilde{\theta}_{ref}$ is the reference indicator value. The diffusion problem (18) along with the appropriate boundary conditions will lead to indicator values of close to 0.0 in domains that are connected to where the Dirichlet boundary condition of $\tilde{\theta} = 0.0$ is applied and indicator values close to 1.0 in disconnected sub-domains. It should be noted that a non-physical "bulk" convection term in Eqn. (18) prevents ill-conditioning of the linear diffusion system even if disconnected sub-domains
exist. After the auxiliary indicator field solution has been obtained, a smoothed Heaviside projection function is used to enforce a 0-1 indicator field. The weak form of the governing equation of the nonlinear structural problem (1) is augmented by the following selective spring stiffness term:

$$\mathbf{R}_{Spr} = \int_{\Omega_S} \delta\mathbf{u}\mathbf{u}\,\mathbf{I}\,r\,E_k\,\bar{\theta}\,dVs \qquad (19)$$

where r is the relative spring stiffness ratio, and E_k is the Young's modulus of either solid material (k = active or passive). For more details regarding selective structural springs, the reader is referred to [34].

In summary, the governing equation in weak form is composed of the following terms which have been introduced above, see (1), (9), (16), (18), and (19):

$$\tilde{\mathbf{R}} = \mathbf{R} + \mathbf{R}_{\Gamma P} + \mathbf{R}^{D} + \mathbf{R}_{Aux} + \mathbf{R}_{Spr} = \mathbf{0} \qquad (20)$$

Formulation of Optimization Problem

The combined LS-XFEM and density approach introduced in Sec. 3.1 describes the geometry and the material distribution in parameterized form. These parameters define the optimization variables $\mathbf{s}$. The optimization problem considered here can be written as follows:

$$\min_{\mathbf{s}} \quad z(\mathbf{s},\mathbf{u}) = z_{tar}(\mathbf{s},\mathbf{u}) + z_{reg}(\mathbf{s})$$

$$\text{s.t. } g_j(\mathbf{s},\mathbf{u}) \le 0 \quad j = 1 \ldots N_g \quad \mathbf{s} \in \Pi = \{\mathrm{R}^{Ns} \,|\, \mathbf{s}_L \le \mathbf{s} \le \mathbf{s}_U\} \quad \mathbf{u} \in \mathrm{R}^{Nu} \qquad (21)$$

where the nodal displacements **u** satisfy the discretized governing equation $\tilde{\mathbf{R}} = \mathbf{0}$ and implicitly depend on the design variables **s**. The number of design variables is denoted by N_s and the number of state variables is N_u. The design variables include both the nodal LS values s^{φ} and the fictitious nodal SIMP densities $s^{\tilde{\rho}}$, such that $s_i = [s^{\varphi}, s^{\tilde{\rho}}]$. The lower and upper bounds of the optimization variables are denoted by $\mathbf{s}_L$ and $\mathbf{s}_U$, respectively. The number of inequality constraints g_j is denoted by N_g. In this work, a nested analysis and design approach (NAND) [35] is used where the displacements **u** are considered dependent variables of **s** and satisfy the governing equations for a given design. The advantage of this approach is that different solution algorithms can be utilized for solving the "forward" analysis problem and the optimization problem. Displacement matching of active structures is the main objective of this work. The first part of the objective function is therefore formulated as a minimization of the squared difference between the nodal displacements **u** and the target displacements $\mathbf{u}_{tar}$ at a specified target set $\Gamma^0_{tar} \subset \Gamma^0$:

$$z_{tar}(\mathbf{s}, \mathbf{u}) = \int_{\Gamma^0_{tar}} (\mathbf{u} - \mathbf{u}_{tar})^2 dA \quad (22)$$

It should be noted that even though a target displacement is specified a priori, no constraints with respect to the required geometry and material layout are imposed. The resulting, in general, non-intuitive geometry and material layout required to achieve a deformation that best matches the target displacements $\mathbf{u}_{tar}$ is solely a result of solving the optimization problem of Eqn. (21). Selecting the target set Γ^0_{tar}, which in this work is defined as a subset of the design domain boundary Γ^0, is
in general non-trivial and highly dependent on the desired target deformation. Mechanical constraints like self-penetration or non-uniqueness of geometric mappings of planar structures onto the desired target deformation need to be considered in order to define a well-posed optimization problem. More details on the target displacements and the corresponding target sets considered in this work are provided in Sec. 5.
In addition to target displacement matching, a regularization term is added to the objective function in order to avoid the emergence of irregular geometric artifacts [11]. Here, regularization is introduced through a perimeter penalty that is formulated as:

$$z_{reg}(\mathbf{s},\mathbf{u}) = \gamma_{per} \int_{\Gamma^0} dA \qquad (23)$$

where γ_{per} is the perimeter penalty factor chosen such that smoothing of the interface geometry is obtained while not allowing Eqn. (23) to dominate the overall objective.
Besides the objective contributions defined in Eqn. (22) and Eqn. (23) two inequality constraints are imposed. The first one is a volume constraint bounding the maximum amount of solid phase allowed within the entire design domain:

$$g_1(\mathbf{s},\mathbf{u}) = \frac{\int_{\Omega^0} S \, d\Omega^0}{\int_{(\Omega_S + \Omega_V)} d\Omega^0} - \gamma_v \leq 0 \qquad (24)$$

where γ_v controls the maximum allowed solid volume Ω^0_S relative to the entire design domain volume $\Omega^0 = \Omega^0_D \cup \Omega^0_V$. To control the stiffness of the structure in the activated state, an end-stiffness constraint is enforced. Following the work initially proposed by [36], it is formulated as:

$$g_2(\mathbf{s},\mathbf{u}) = \frac{S' - S}{S} - \gamma_s \leq 0 \qquad (25)$$

where S is the strain energy of the system after activation (with no external load applied) and S' is the strain energy after applying an additional external perturbation load. The limit in relative amount of change in strain energy with and without the final perturbation load is denoted by γ_s. The end-stiffness constraint therefore requires a certain stiffness of the structure in the activated configuration in order to resist the perturbation pressure applied in the opposite direction of the desired deformation.

Design Sensitivity Analysis using the Adjoint Method

Due to a large number of design variables, the design sensitivities of objective and constraints are computed using the adjoint method. Since the mechanical model is static and conservative, the adjoint problem only needs to be solved at the end of the loading process [37]. When the end-stiffness constraint is enforced, the design sensitivities for the displacement matching objective need to be evaluated at the load increment t_{Load} while the sensitivities for the end-stiffness constraint are evaluated at t_{Pert} .

Following the work of [24, 38], the derivative of the objective z with respect to the vector of design variables $\mathbf{s}$ for a quasi-static case is:

$$\frac{dz}{d\mathbf{s}} = \frac{\partial z}{\partial \mathbf{s}} + \frac{\partial z}{\partial \mathbf{u}}^{T} \frac{d\mathbf{u}}{d\mathbf{s}} \tag{26}$$

where the first term represents explicit dependencies while the second term represents the implicit sensitivities. Considering the two sets of nodal design variables, $\mathbf{s}^{\varphi}$ and $\mathbf{s}^{\tilde{\rho}}$, and the filtering and projection relationships defined in Sec. 3.1, the total

derivative of (26) can be further expanded into:

$$\frac{d\mathbf{u}}{d\mathbf{s}} = \frac{\partial \mathbf{u}}{\partial \varphi}\frac{d\varphi}{d\mathbf{s}^{\varphi}} + \frac{\partial \mathbf{u}}{\partial \hat{\rho}^{e}}\frac{\partial \hat{\rho}^{e}}{\partial \tilde{\rho}^{e}}\frac{\partial \tilde{\rho}^{e}}{\partial \rho^{e}}\frac{\partial \rho^{e}}{d\mathbf{s}^{\tilde{\rho}}} \tag{27}$$

Satisfying the governing equation (20) for every design, i.e. $\tilde{\mathbf{R}} = \mathbf{0}$, the derivative $d\mathbf{u}/d\mathbf{s}$ can be computed from:

$$\frac{d\tilde{\mathbf{R}}}{d\mathbf{s}} = \frac{\partial \tilde{\mathbf{R}}}{\partial \mathbf{s}} + \frac{\partial \tilde{\mathbf{R}}}{\partial \mathbf{u}}\frac{d\mathbf{u}}{d\mathbf{s}} = \mathbf{0} \tag{28}$$

Solving Eqn. (28) for $d\mathbf{u}/d\mathbf{s}$ and combining it with Eqn. (26) yields:

$$\frac{dz}{d\mathbf{s}} = \frac{\partial z}{\partial \mathbf{s}} - \frac{\partial z}{\partial \mathbf{u}}\left(\frac{\partial \tilde{\mathbf{R}}}{\partial \mathbf{u}}\right)^{-1}\frac{\partial \tilde{\mathbf{R}}}{\partial \mathbf{s}} \tag{29}$$

where the following adjoint problem can be identified:

$$\left(\frac{\partial \tilde{\mathbf{R}}}{\partial \mathbf{u}}\right)^{T}\lambda = \frac{\partial z}{\partial \mathbf{u}} \tag{30}$$

The adjoint solution is denoted by λ, which is used to finally compute the expression for the design sensitivities as:

$$\frac{dz}{d\mathbf{s}} = \frac{\partial z}{\partial \mathbf{s}} - \lambda^{T}\frac{\partial \tilde{\mathbf{R}}}{\partial \mathbf{s}} \tag{31}$$

It should be noted that in the current work, the explicit contribution $\partial z/\partial \mathbf{s}$ and the post-multiplication term $\partial \tilde{\mathbf{R}}/\partial \mathbf{s}$ are obtained via finite differences on an elemental level. In a similar fashion as discussed above, the design sensitivities of the constraints with respect to the design variables can be obtained. For more details regarding the computation of design sensitivities with the XFEM, the interested reader is referred to [39].

Validation of the Hyperelastic Thermomechanical Model

The finite deformation thermomechanical model introduced in Sec. 2 is validated against experimental results and an analytical beam model to establish confidence in the XFEM model for design optimization. The test specimen for model

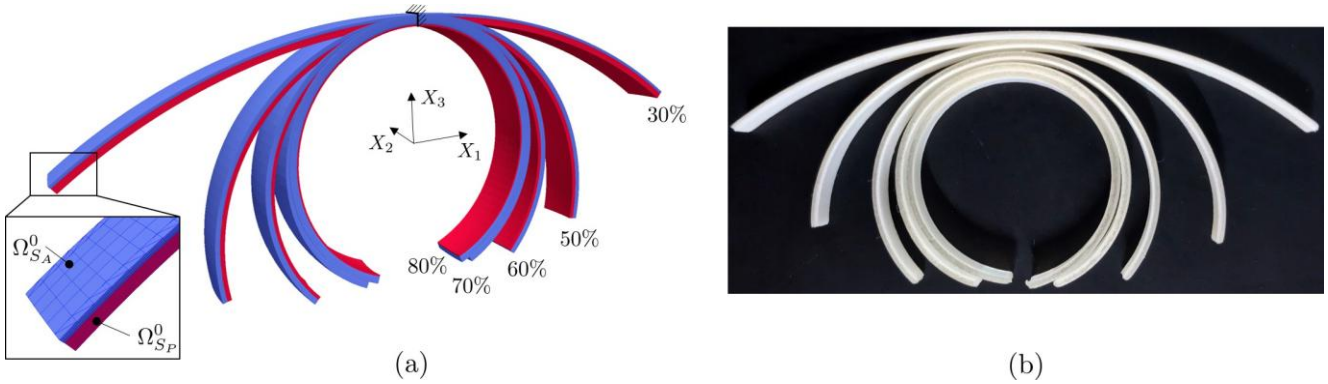


Fig. 4. Bi-layer strips with different active material ratios (in %) used for XFEM model validation. The solid-void interface of the strips along the X_1 axis is cut by the XFEM and tetrahedralized for volume integration. (a) Simulation results and (b) experimental results.

Table 1. XFEM model of bi-layer validation strips.

Dimensions	$80.0 \times 5.0 \times 1.0$ *mm*
Mesh Size	$80 \times 5 \times 10$
Weak BC Penalty	$\gamma_D = 250.0$
Prescribed Thermal Load	$\bar{T} = 1.0$ K
Reference Temperature	$T_0 = 0.0$ K

Table 2. Material parameters of Tango+ and Vero.

Young's Modulus Tango+	$E_T = 0.6$ MPa	Young's Modulus Vero	$E_V = 8.0$ MPa
Printing Strain Tango+	$\alpha_T = 0.05\ ^{1}/_{K}$		
Printing Strain Vero	$\alpha_V = 0.0\ ^{1}/_{K}$		
Poisson Ratio of Tango+, Vero	$\nu_T = \nu_V = 0.4$		

validation are rectangular, bi-layer strips with different volume ratios of active versus passive material, leading to different curvature values. The bi-layer composite is made out of *Tango+* as the active elastomer in the top layer (Ω^{0}) and *Vero* as the passive glassy polymer in the bottom layer (Ω^{0}) printed on a Stratasys Keshet J750 multi-material 3D printer, with a printing layer thickness of 27 μm. The XFEM predictions of the bi-layer strips are shown in Fig. 4 (a) while the printed and
activated specimen are shown in Fig. 4 (b).

The model parameters and the material parameters of the XFEM model are given in Tables 1 and 2 respectively. Only one quarter of the domain is simulated and mechanical symmetry boundary conditions are applied along the X_1 and X_2 plane using the weak boundary condition formulation stated in Eqn. (16). The XFEM is used to describe the solid-void boundary of the bi-layer strips along the X_1 axis as highlighted in the insert in Fig. 4 (a). Note that the void domain is not shown in Fig. 4 (a) for clarity. This approach replicates a non-conforming mesh for analyzing the solid domain just as it is present during the subsequent design optimization process. The varying volume fraction of active material (*Tango+* represented in blue in the top layer) and passive material (*Vero* represented in red in the bottom) is modeled by uniformly changing the material ratios respectively. The computational mesh consists of 1630 HEX20 XFEM elements of which 400 are intersected resulting in a total of 26,227 DOFs. HEX20 elements are 20 node hexahedral serendipity elements with a total of 60 DOFs. The bending behavior of the bi-layer strips due to different thermal expansion of the layers is studied for five distinct volume fractions of active material. The curvature is measured at the mid-plane of the strips in the X_2 symmetry plane. A

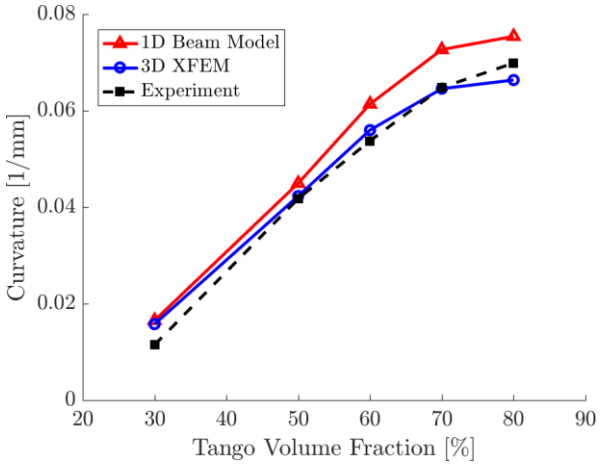


Table 3. XFEM model parameters for design optimization problems.

Dimensions (Quarter Domain)	$80.0 \times 80.0 \times 1.0$ *mm*
Mesh Size (Quarter Domain)	$32 \times 32 \times 10$ Weak BC Penalty $\gamma_D = 250.0$
Prescribed Thermal Load	$\bar{T} = 1.0$ K
Reference Temperature	$T_0 = 0.0$ K

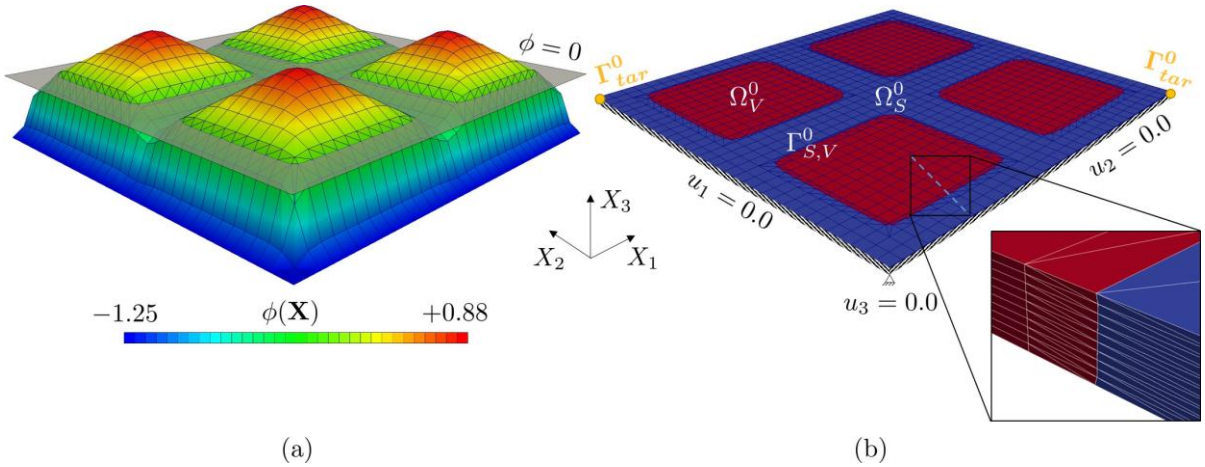
comparison of the curvature values obtained by the 3D XFEM model, a 1D Timoshenko beam model as outlined in [5] and physical experiments for different *Tango+* volume fractions is presented in Fig. 5. It should be noted that due to a small sample size of 8 samples per volume fraction, error bars are not meaningful and therefore omitted when plotting the mean curvature in Fig. 5. Good agreement is achieved between the 3D XFEM model and the physical experiments, whereas the 1D model tends to overestimate the curvature, especially for large volume fractions of *Tango+*. This is due to assumptions made by the Timoshenko beam model which do not account for Poisson effect as well as transverse thermal expansion. Both of those phenomena are, however, present in the physical experiments where a double curvature (i.e. cylindrical bending) is observed for *Tango+* volume fractions greater than 50%. These phenomena are accurately captured in the 3D XFEM model where the curvature along the X_1 direction is in fact reduced due to an increasing effect of curvature along the X_2 direction.

Design Optimization Examples

The proposed design methodology for finding the optimal design of 4D printed active structures is applied to four design problems. The LSF and the nodal densities for all design examples are discretized using trilinear shape functions. The material properties are approximated element-wise constant and are obtained using an elemental average of all nodal fictitious density values (12) together with the SIMP power law (11). In this work, $\beta = 3.0$ is used for interpolating the
Young's modulus and CTE while $\beta = 1.0$ is used for interpolating the physical density. The values of the SIMP exponent β
have been chosen such that a good convergence towards either active or passive material is achieved.
The projection (13) is applied through a continuation approach which represents a trade-off between convergence be-

havior and computational efficiency of the optimization process. Initially, the projection threshold parameter is set to $\eta = 0.5$ and the sharpness parameter is $\gamma = 0.01$. After a converged initial design is obtained, (e.g. after 100 design iterations), the sharpness parameter is increased to $\gamma = 3.0$ and the end-stiffness constraint is enforced. The projection sharpness parameter is then doubled every 100 design iterations. This procedure is repeated four times until $\gamma = 48.0$ and a sufficient approximation to a bi-material design within the solid domain is obtained. After the overall geometry has converged to an optimum (e.g.
after 100 design iterations), the LS design variables stay unchanged while the material distribution within the solid domain is further optimized, to yield a bi-material design with a certain end-stiffness. For both sets of design variables (nodal LS
values s^{φ} and nodal fictitious densities $s^{\tilde{\rho}}$), a smoothing radius of $r_s = 4.0$ *mm* is used.

The optimization problem (21) is solved using the gradient-based nonlinear programming scheme Globally Convergent



(a) (b)

Table 4. Optimization problem parameters.

Perimeter Penalty	$\gamma_{per} = 5.0 \cdot 10^{-2}$
Lower bound for LS design variables	$\mathbf{s}^{\varphi} = -1.25$
Upper bound for LS design variables	$\mathbf{s}^{\varphi} = +1.25$
Lower bound for density design variables	$\mathbf{s}^{\tilde{\rho}} = 0.0$
pper bound for density design variables	$\mathbf{s}^{\tilde{\rho}}$
GCMMA initial asymptote adaption parameter	0.5
GCMMA asymptote adaption parameter	0.7
	1.0

Method of Moving Asymptotes (GCMMA) [40] without inner iterations. The respective parameters of the optimization problem are listed in Tab. 4. The optimization problem is considered converged once a relative residual norm drop of the Karush - Kuhn - Tucker (KKT) conditions [41] greater $1.0 \cdot 10^{10}$ is achieved and all constraints are satisfied.

For all examples, the initial design is a flat square plate composed of uniform, intermediate material of density $\mathbf{s}\tilde{\rho} = 0.5$ in Ω^0 with an initial seeding of square holes representing Ω^0, see Fig. 6 (b). The size of the cuboid inclusions is

$S \quad V$

$\mathbf{r}_i = [14.5, 14.5, 14.5]$ *mm* for all examples. Different target displacements are prescribed to certain subsets of the domain boundary Γ^0 in order to achieve target deformations of varying complexities. A design with the desired mechanical response is found through optimizing the solid-void geometry as well as the active-passive material distribution within the solid

domain by solving the optimization problem outlined in Sec. 3.4. The material properties used for all design examples are listed in Tab. 2 and parameters specific for each design example are listed in Tab. 5.

For all subsequent design problems, quarter symmetry of the mechanical problem about the X_1 and the X_2 plane is exploited by analyzing only one quarter of the design domain and enforcing appropriate mechanical boundary conditions weakly via Nitsche's method (16). In addition, for the design problems of Sec. 5.2, Sec. 5.3, and Sec. 5.4, design symmetry about the $X_1 - X_2$ diagonal is introduced by assigning a set of independent nodal LS values and nodal fictitious density values to only one eighth of the total design domain. The initial design used for all design optimization examples along with the

symmetry boundary conditions is depicted in Fig. 6 (b).

The LSF of the initial design is shown in Fig. 6 (a) and computed as a signed-distance function from an array of cuboids defined as:

$$\varphi(\mathbf{X}) = 1 - \min_i \left(\left(\frac{X_1 - \tilde{X}_{1_i}}{r_{1i}} \right)^n + \left(\frac{X_2 - \tilde{X}_{2_i}}{r_{2_i}} \right)^n + \left(\frac{X_3 - \tilde{X}_{3_i}}{r_{3_i}} \right)^n \right)^{\frac{1}{n}} \tag{32}$$

where i is the number of individual cuboids, $\mathbf{r}_i$ is the radius of the i-th cuboid, and $\tilde{\mathbf{X}}_i$ is the position of the center of the i-th cuboid in X_1, X_2 and X_3 direction respectively. The roundness parameter is set to $n = 100.0$. The parameters of this arbitrary initial design have been determined through numerical studies to minimize the dependence of the final design on the initial

geometry.

The plane creating the zero LS iso-contour is shown in gray (Fig. 6 (a)) and the corresponding solid-void material layout is depicted in Fig. 6 (b). It should be noted that LS design variables are only defined on the top surface of the initially flat plate, such that $\varphi(X_1, X_2, X_3) = \varphi(X_1, X_2)$. The LS values of all nodes which are not on the upper surface are dependent on the corresponding design variable hosted by the respective node on the top surface. This guarantees to always have a vertical

cut in X_3 direction represented by the XFEM (see insert in Fig. 6 (b)) and it prevents the optimizer from locally

reducing the plate thickness during the optimization process.

The target displacements are monitored at target sets Γ^0 defined at the tips of the structure (along the symmetry boundaries). To guarantee that these tips are mechanically connected to the base of the structure, the LS field along the symmetry boundaries is fixed to be negative (see Fig. 6 (a)). This means, strips along the symmetry boundaries are

excluded from the LS-XFEM design domain and remain solid throughout the optimization process.

However, regarding the density optimization, this domain is still considered design domain in which the material distribution can be altered.

The nonlinear thermomechanical model is discretized by quadratic HEX20 XFEM elements. While the in-plane dis-cretization varies for each example, 10 HEX20 brick elements are used for discretization in thickness direction in order to accurately capture the bending behavior of the slender structures and to avoid shear locking exhibited by lower-order brick elements. An iterative Newton-Raphson scheme is used to solve the nonlinear problem that is considered as converged when a relative nonlinear residual norm drop greater $1.0 \cdot 10^{6}$ is achieved. Convergence is facilitated by the adaptive load-stepping

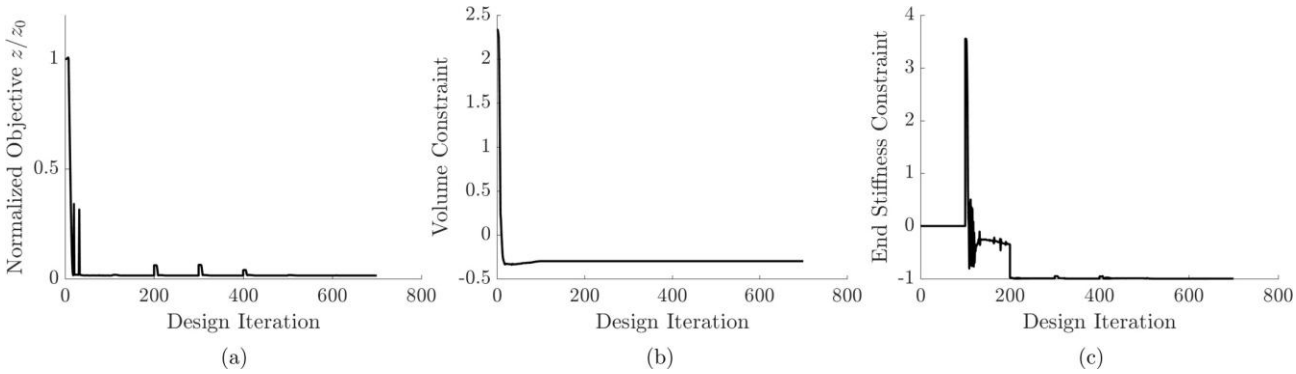
Table 5. Parameters used for each design example.

	Twisted Figure-Eight	Cylinder Gripper	Four-Legged Gripper	Elevated Plane
Initial Void Pattern	$4 \times 4 \times 1$	$4 \times 4 \times 1$	$4 \times 4 \times 1$	$6 \times 6 \times 1$
Volume Constraint γ_v	0.15	0.20	0.10	0.10
Change in Strain Energy γ_s	$5.0 \cdot 10^{-5}$	$5.0 \cdot 10^{-5}$	$1.0 \cdot 10^{-6}$	$5.0 \cdot 10^{-5}$
Perturbation Pressure $\bar{P}$	1.0 *Pa*	0.1 *Pa*	1.0 *Pa*	1.0 *Pa*
GCMMA Step Size	0.04	0.03	0.03	0.03

method covered in Section 2.2, where the maximum number of nonlinear iterations is set to 40 and the time step reduction factor is set to f = 0.25. Once again, it is important to stress how crucial the adaptive load-stepping method is to the nonlinear problem's convergence throughout the optimization phase. Adaptively lowering the load step is essential to enable Newton-Raphson scheme convergence, particularly for designs including significant quantities of weak material, that is, material with intermediate densities. The Multifrontal Massively Parallel Solver (MUMPS) is used to solve the linearized sub-systems [42, 43].

The converged nonlinear solution of the state variables of the prior design is used as an initial estimate for evaluating the current design in order to increase the computational efficiency of the optimization strategy. This method works effectively for issues involving incremental design modifications and static conservative mechanical models where the displacement behavior of the old design and the displacement solution of the present design vary only marginally [44]. The design is examined by simulating the whole load path if the design change and the ensuing change in the displacement response are too significant, i.e., no equilibrium configuration is found using the converged solution of the prior design as a starting estimate. Selective structural springs, as described in Section 3.3, are utilized to stabilize unconnected solid sub-domains throughout the optimization process. In this supplementary diffusion issue, $\kappa = 10.0$ is the thermal conductivity, $h = 0.01$ is the bulk heat transfer coefficient, and θ geometre $f = 1.0$ is the reference indication value. A relative spring stiffness ratio of $r = 1.0 \cdot 10{-}6$ is used, and a uniform starting indication value of $\theta 0 = 1.0$ is applied to the whole domain. On borders when no displacements are specified, adiabatic boundary conditions on the auxiliary indicator field are assumed. A staggered solution methodology is used to further enhance the suggested method's numerical stability. The nonlinear thermomechanical issue (1) is handled in a one-way coupled fashion after the linear diffusion problem of the auxiliary indicator field (18) is resolved. The direct 4D printing technique presented by [5] is used to

construct and activate the final design for each example issue. Tango+ and Vero material are precisely deposited into a build tray using a Stratasys Keshet J750 multi-material 3D printer in order to fabricate the optimum shape-changing structures, as explained in Sec. 4. The solid-void border of the final design is recovered using the zero LS iso-contour, and different active and passive material domains are generated by extracting an iso-volume along a fictional density threshold of ρΨe = 0.5. Because ParaView offers an easy interface between the ExodusII mesh format and other computer-aided design (CAD) file formats, it is used for these post-processing procedures [45]. For each material sub-domain in the present study, a stereo-lithography (STL) mesh file is retrieved from the convergent optimization result (given in ExodusII format by the used LS-XFEM optimization framework). The CAD data is imported into the Stratasys printing program using the STL file format, which is often supported by 3D printing software. Tango+ is allocated to the active material domain ($0 \leq \rho_e < 0.5$) in the Stratasys pre-processing environment, while Vero is assigned to the passive material domain ($0.5 \leq \rho_e \leq 1$). Only when the inelastic printing strain in the Tango+ material is released do the active structures, which are printed in a flat shape, deform. This is caused by immersing the originally flat, bi-material constructions in a water bath at 65.0°C, which softens the stiffer Vero material because of its glass transition temperature, which is around 53.0°C. This enables Tango+'s inherent compressive printing strain to be relieved, changing its form. Once the structure has cooled to normal temperature, the distortion becomes permanent. The activation procedures and the direct 4D printing method are covered in further depth in [5].
Note that as a quantitative comparison is beyond the purview of this work, all experimental findings are presented only for qualitative comparison. The experimental verifications indicate that the numerically determined designs are feasible and that the suggested design framework may be used to systematically solve real-world design issues.



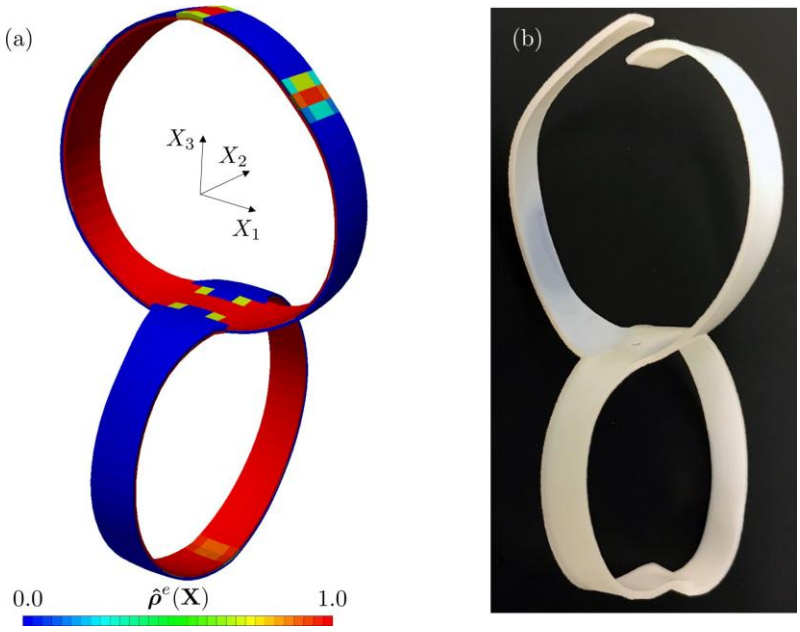


Fig. 8. Final design of the twisted figure-eight example in deformed configuration. (a) XFEM prediction and (b) activated 4D printed sample. In the printed sample, *Tango+* is transparent and *Vero* is white.

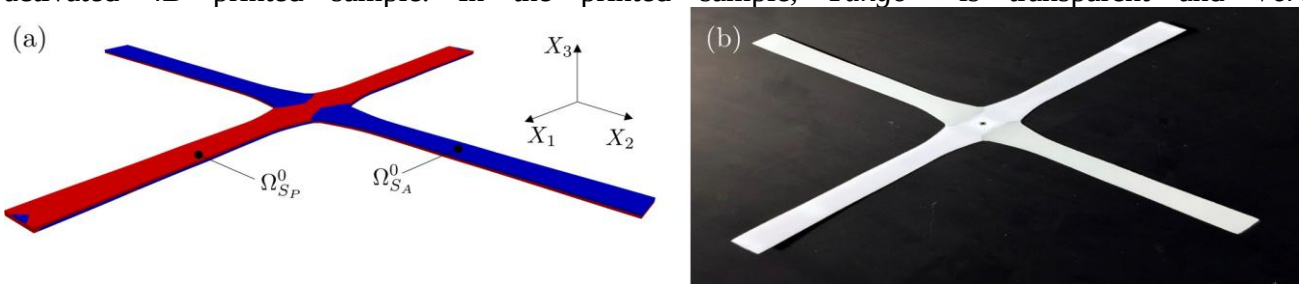


Fig. 9. Final twisted figure-eight design in undeformed configuration, (a) extracted material phases and (b) printed structure.

A slight overlap of the tips of the four legs is seen in the numerical prediction. This is due to the lack of a self-contact formulation which is beyond the scope of this work. Intuitively, a perfectly symmetric design is expected in order to meet the twisted figure-eight target deformation. A slight asymmetry can, however, be observed in Fig. 8, for both the XFEM simulation and the physical experiment. This is attributed to a local minimum identified by the GCMMA during the design optimization process. The increasing projection parameter then locks the design into this local minimum as the design space becomes increasingly more non-convex with a higher projection parameter γ.

The evolution of the normalized objective z/z_0, where z_0 is the objective value of the initial design, the volume constraint (24) and the end-stiffness constraint (25) are shown in Fig. 7 for this first design optimization example. A similar behavior is also observed for all other numerical examples. After initial oscillations in the objective, which are due to the violation of the volume constraint, a smooth and converging behavior is seen. The slight increase of the objective every 100 iterations is due to an increasing projection parameter γ which makes the design space increasingly more nonlinear. Therefore, the optimization algorithm needs a few design iterations to minimize the objective again until convergence is obtained. It is observed that even though initially the volume constraint is active, it becomes inactive within the first 20 design iterations. The motivation for the solid strips to become thinner is to reduce the effect of double curvature due to the isotropic inelastic printing strain which impedes on the primary bending behavior. Therefore,

the volume constraint stays inactive for the remainder of the optimization process. As mentioned before, the end-stiffness constraint is not enabled during the first 100 design iterations. Once enabled, it is initially violated but quickly becomes inactive after about 50 design iterations. Using the smoothed Heaviside projection in combination with the end-stiffness constraint greatly benefits the final stiffness of the structure as intermediate material is mitigated with an increasing projection parameter γ.

Fig. 9 (a) shows the final design in the undeformed configuration after two distinct material phases have been extracted in a post-processing step. In the current and in future examples, *Tango+* is printed transparent while *Vero* is printed in either white or magenta, see Fig. 9 (b). Overall, this example shows a first application of the proposed method and it demonstrates that desired target deformations can be achieved upon activation of an initially flat, plate-like structure.

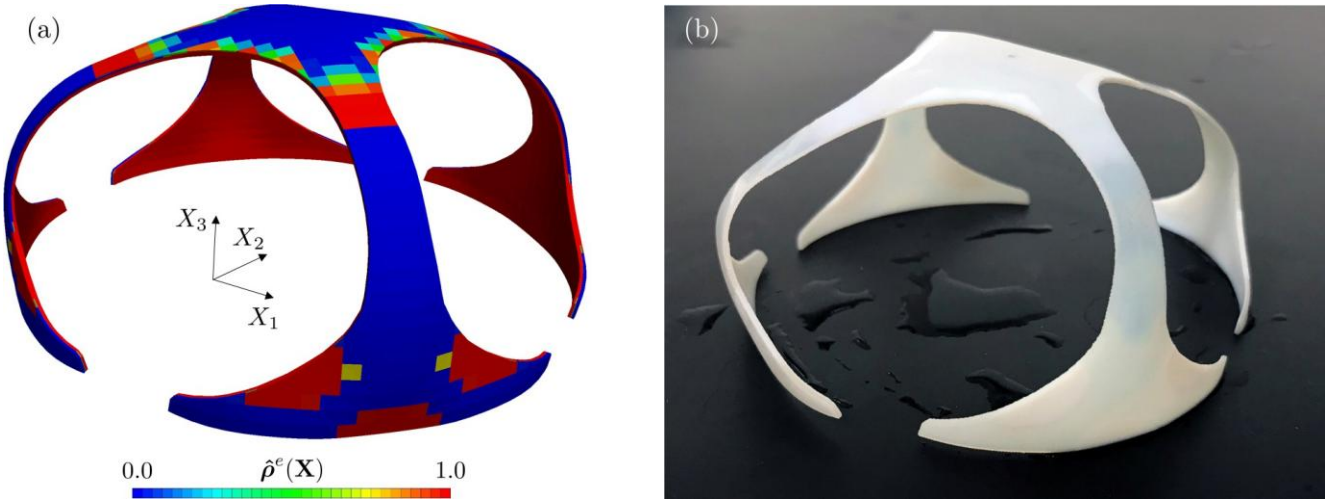


Fig. 10. Final design of the cylinder gripper in deformed configuration. (a) XFEM prediction and (b) activated experiment where *Tango+* is transparent and *Vero* is white.

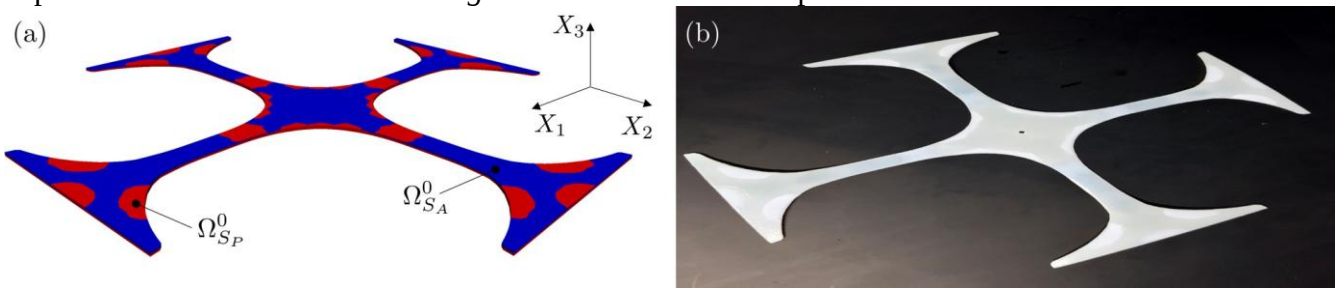


Fig. 11. Final cylinder gripper design in undeformed configuration, (a) extracted material phases, (b) printed specimen.

Cylinder Gripper Example

A similar design study as performed in Sec. 5.1 is repeated for finding the optimal design of an initially flat structure which deforms into a gripper enclosing a cylinder as its target. The target displacement of the gripper is monitored at the target set Γ^0_{tar} which is comprised of $\mathbf{X}_1 = [0 \leq X_1 \leq 30.0, 75.0 \leq X_2 \leq 80.0, -0.5]$ *mm* and $\mathbf{X}_2 = [75.0 \leq X_1 \leq 80.0,\ 0 \leq X_2 \leq 30.0, -0.5]$ *mm* spanning the tips of the gripper. The desired deformation of the tips of the structure is described by a surface of a cylinder aligned with the X_3 axis, with radius $R_{tar} = 50.0$ *mm* and a depth of $X_{3tar} = -45.0$ *mm*. The XFEM model parameters listed in Tab. 3 are used. Parameters specific to this example are found in Tab. 5.

A smooth evolution of objective and constraints is observed as discussed before. The convergence history plots are omitted here for brevity. Fig. 10 shows the final design (a) in the deformed configuration next to (b) the experimental

result for the cylinder gripper. Qualitatively, the structure fabricated and activated through direct 4D printing assumes the anticipated target deformation well. From the predicted XFEM simulation it can clearly be seen that the optimizer took advantage of the possibility to use double curvature in order to achieve the cylindrical target deformation. Moreover, a non-uniform curvature in the outward pointing legs is used to best match the target deformation at the tips of the gripper. The optimal curvature is controlled by the amount of stiff, passive *Vero* material along the top of the gripper (shown in red). Pure *Vero* is also placed as fillets at the tips of the gripper to control the bending behavior and to also contribute towards a higher stiffness of the overall structure.

In Fig. 11 the corresponding initial, flat configuration of the optimal design is shown. As before, distinct material phases were extracted from the final fictitious density field in a post-processing step; see Fig. 11 (a). Fig. 11 (b) shows the printed physical specimen for the self-deforming cylinder gripper. This example successfully demonstrates that the proposed design method is not limited to finding the optimal geometry of simple target deformations, but also handles more sophisticated ones. Non-uniform double curvature is used in the optimized gripper design to obtain the desired deformation upon activation.

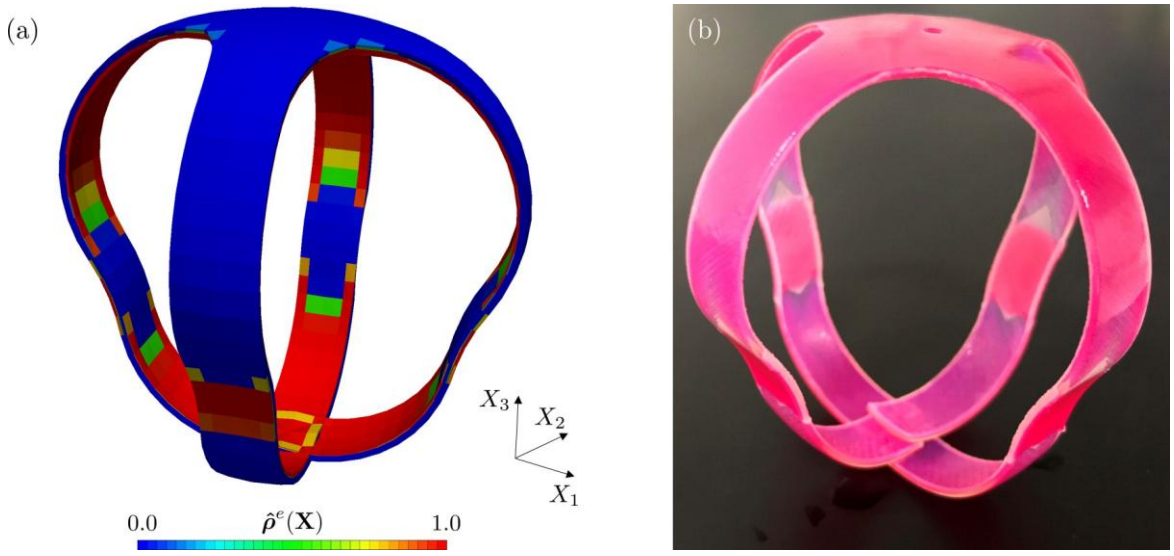


Fig. 12. Final design of the four-legged gripper example in deformed configuration. (a) XFEM prediction, (b) activated experiment. In the printed specimen, *Tango+* is transparent and *Vero* is magenta.

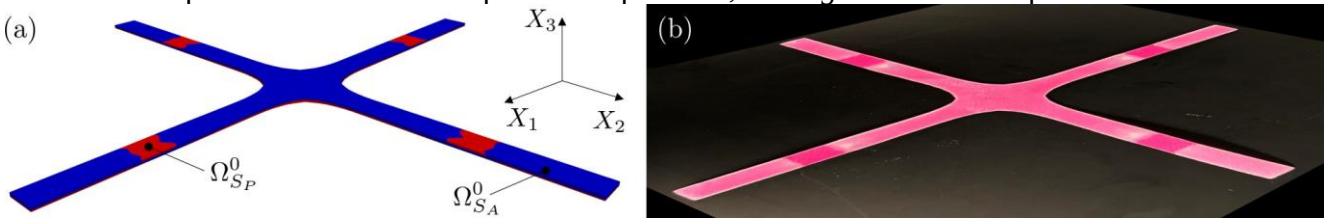


Fig. 13. Final four-legged gripper design in undeformed configuration, (a) extracted material phases and (b) printed sample.

Four-Legged Gripper Example

The third design optimization example aims to create an active four-legged gripper. The target displacement is designed to mimic grasping an item. This is accomplished by defining a goal displacement of utar = [−80.0, 0.0, −50.0] mm at X1 = [0.0, 80.0, 0.0] mm and prescribing a comparable target displacement of utar = [0.0, −80.0, −50.0] mm at X2 = [80.0, 0.0, 0.0] mm. A structure where all four goal points meet in the design domain's center underneath its original, flat shape is described by this target displacement. The parameters unique to this four-legged

gripper example are found in Tab. 5, whereas the XFEM model parameters stated in Tab. 3 are employed as in earlier instances.

Fig. 12 shows both (a) the XFEM prediction and (b) the physical sample of the four-legged gripper in the ideal design layout in the deformed configuration. This design challenge displays design phenomena that were not previously seen in Sections 5.1 and 5.2 because of the target deformation's increasing complexity. The gripper's final design comprises of four legs that nonintuitively deform to match the intended deformation. Convex-concave curvature sections are made to improve the stiffness of the four legs because an end-stiffness restriction is imposed. These intriguing characteristics show how a meaningful, intricate active gripper structure is produced by geometry features that are activated by a mechanical stiffness restriction. The bottom center of the construction exhibits self-penetration of all four gripper legs due to the legs' limited breadth. This results from the XFEM model's incapacity to take touch into account. By overlapping the four gripper legs at various X3 depths, self-penetration is prevented in the physical experiment. However, future research should include interaction to better explain a behavior such as this. Overall, there is strong qualitative agreement between the direct 4D printed four-legged gripper and the XFEM forecast.

The comparable original, undisturbed design for the four-legged gripper is seen in Fig. 13. The printed specimen (Fig. 13 (b)) and the XFEM model (Fig. 13 (a)) both show the separate areas of convex-concave curvature where the bi-layer beam composition is locally reversed at around the halfway point of each gripper leg.

Elevated Plane Example

The last example used to demonstrate the capabilities of the proposed multi-material topology optimization framework is the design of a self-elevating plane. For this design example, the domain size is increased to $120.0 \times 120.0 \times 1.0$ *mm* for the quarter domain. This increase in in-plane domain size improves the ability to capture double curvature with the given eigenstrain provided by the active material. A mesh size of $48 \times 48 \times 10$ elements is used to discretize one quarter of the design domain, leading to initially 276,000 free DOFs. To achieve self-elevation of the domain in the center of the design space by 40.0 *mm* in the X_3 direction, a target displacement of $\mathbf{u}_{tar} = [0.0, 0.0, +40.0]$ *mm* is defined at the center of the domain spanned by $\mathbf{X}_1 = [0.0 \leq X_1 \leq 15.0, 0.0 \leq X_2 \leq 15.0, 0.0]$ *mm*. In addition, the out-of-plane displacement is fixed at

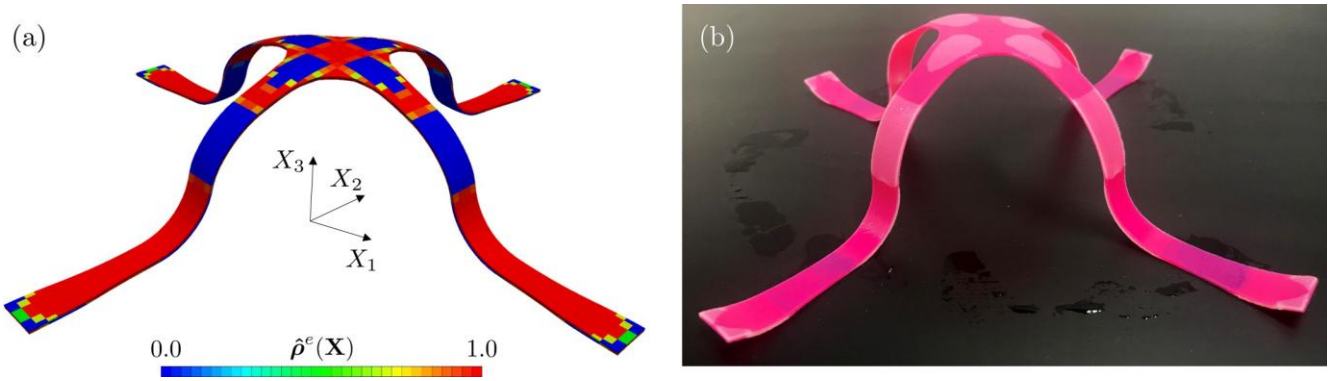


Fig. 14. Final design of the self-elevating plane in the deformed configuration. (a) XFEM prediction and (b) direct 4D printed specimen. In the printed sample, *Tango+* is transparent and *Vero* is magenta

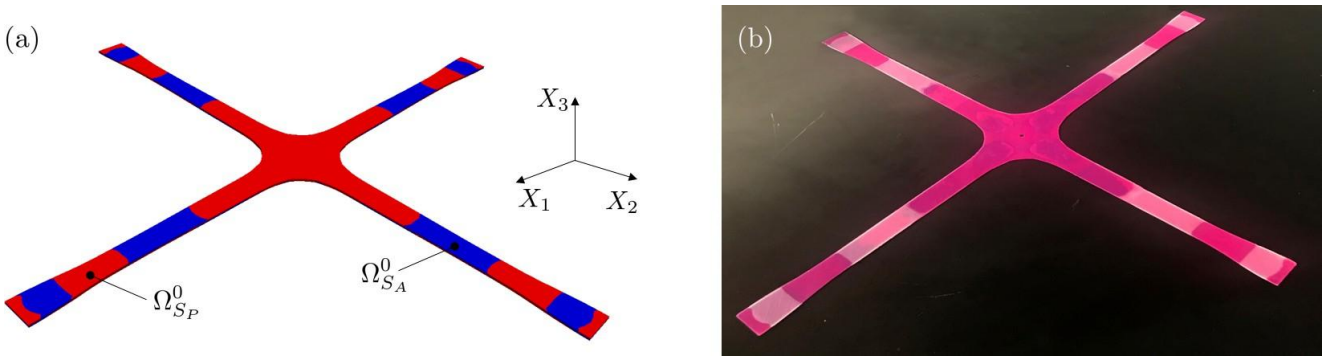


Fig. 15. Final elevated plane design in undeformed configuration, (a) extracted material phases and (b) printed sample.

X1 = [105.0 ≤ X1 ≤ 120.0, 0.0 ≤ X2 ≤ 5.0, 0.0] mm and X2 = [0.0 ≤ X1 ≤ 5.0, 105.0 ≤ X2 ≤ 120.0, 0.0] mm define the tips along the symmetry planes. Tab. 3 lists the remaining XFEM model parameters for this example, whereas Tab. 5 lists all additional problem-specific parameters. Fig. 14 shows the self-elevating plane's final design in the distorted state. The direct 4D printed physical specimen and (a) the XFEM prediction are both shown. In both the actual experiment and the simulation, the desired deformation is successfully attained. It creates a cross-shaped structure that is fastened to the platform in the middle. When activated, the non-uniform active-passive material architecture of each cross member produces different regions of concave-convex bending. In order to raise the structure's center in the X3 direction without causing any out-of-plane displacement or rotation at the points, this curvature adjustment is required. The undisturbed raised plane structures corresponding to (a) the XFEM simulation and (b) the printed sample before to activation are shown in Fig. 15. The active and passive material domains needed for direct 4D printing are clearly identified and any residual intermediate densities are eliminated using a thresholding approach.

Conclusions

For constructing direct 4D printed, shape-changing structures suffering significant deforestations, a topology optimization method was put out. The multi-material optimization issue was described using a combined LS-XFEM and density-based topology optimization technique. The solid-void domains were clearly described using the LS-XFEM, and the solid domain's active and passive material sub-domains were differentiated using the SIMP technique. An XFEM formulation was used to discretize the hyperelastic thermomechanical model utilizing quadratic displacement elements. A residual isotropic eigenstrain was used to represent the inelastic printing strain brought forth by the direct 4D printing method. Numerical findings were compared with physical tests and an analytical beam model to confirm that the proposed large strain thermomechanical XFEM model accurately predicted the behavior of self-deforming structures. Four sample issues were used to illustrate the possibilities of the suggested design optimization technique. To ensure the final design's structural integrity, the goal was to meet a specified target displacement while adhering to volume and end-stiffness constraints. The suggested framework was successfully used to produce optimal designs that matched goal displacements of a twisted figure-eight design, a cylinder gripper, a four-legged gripper, and a self-elevating plane. To satisfy the end-stiffness restriction, more complicated geometries and material arrangements were developed that exploit mechanical phenomena including double curvature, locally concave-convex curvatures, and regions of uniform passive material. There are a few issues that need to be fixed in further work once the suggested framework's design capabilities have been shown. These include the oversimplifications of structural instabilities, which often occur in thin constructions and include buckling and snap-through. Although the use of suitably thick structures in the current study has prevented these structural instabilities, they should be taken into account generally when the active material causes significant compressive stresses in the structure. Previous studies in the subject of modeling slender structures using eigenstrains include [44] and [46], with [46] and [47] in particular taking into account completely nonlinear behavior, including instabilities. Future research should examine how structural instabilities affect the best design of 4D printed structures and create a methodical optimization strategy to either take use of them as a desirable design feature or steer clear of them to improve design robustness.

Furthermore, since the used XFEM framework lacked a self-contact formulation, the third example underwent a considerable degree of self-penetration during the activation step. Future research must also address the integration of an XFEM contact formulation with multi-material topology optimization, as examined by [20], into the suggested design framework. An first example of a methodical design methodology for 4D printed structures suffering significant deformations has been shown in this work. Future research should also examine design issues with more intricate target displacements. Direct 4D printing was used to create the physical specimens for each design sample. The physical reaction and the XFEM prediction showed qualitatively high agreement upon activation. The viscosity of the water bath on the soft structures during the activation process, small anisotropy of the material characteristics with respect to the print direction, and environmental influences like gravity are the major causes of discrepancies between the computational findings and the tests. This study has not taken into consideration any of those physical implications. However, all of those influences should be taken into consideration in further research to improve the consistency between XFEM simulations and 4D printed specimens.

References

[1] Tibbits, S. (2014). "4D printing: Multi-material shape change." Architectural Design, 84(1), pp. 116–121.
[2] Ge, Q., Qi, H. J., and Dunn, M. L. (2013). "Active materials by four-dimension printing." Applied Physics Letters, 103(13), p. 131901.
[3] Ge, Q., Qi, H. J., and Dunn, M. L. (2013). "Active materials by 4D printing." Applied Physics Letters, 103(13), p. 131901.
[4] Maute, K., Tkachuk, A., Wu, J., Jerry Qi, H., Ding, Z., and Dunn, M. L., "Level Set Topology Optimization of Printed Active Composites." Journal of Mechanical Design, 137(11), p. 111402, 2015.
[5] "Direct 4D printing via active composite materials." Science Advances, 3(4). Ding, Z., Yuan, C., Peng, X., Wang, T., Qi, H. J., and Dunn, M. L., 2017.
[6] Zhao, Z., Wu, J., Mu, X., Chen, H., Qi, H. J., and Fang, D. (2017). Macromolecular Rapid Communications, 38(13), p. 1600625. "Desolvation Induced Origami of Photocurable Polymers by Digit Light Processing."
[7] Zhao, Z., Wu, J., Mu, X., Chen, H., Qi, H. J., and Fang, D. (2017). "Origami by frontal photopolymerization." Science Advances, 3(4).
[8] Weeger, O., Yeung, S.-K., Kang, Y. S. B., and Dunn, M. L., "Optimal Design and Manufacture of Active Rod Structures with Spatially Variable Materials." 3D Printing and Additive Manufacturing, 3(4), pp. 204–215, 2016.
[9] Ding, Z., Weeger, O., Qi, H. J., and Dunn, M. L. (2018). "4D rods: 3D structures via programmable 1D composite rods." Materials and Design, 137, pp. 256–265.
[10] Tolley, M. T., Felton, S. M., Miyashita, S., Aukes, D., Rus, D., and Wood, R. J. (2014). "Self-folding origami: Uniform heating activates shape memory composites." Smart Materials and Structures, 23(9), p. 94006.
[11] Van Dijk, N. P., Maute, K., Langelaar, M., and Van Keulen, F. (2013). "Level-set methods for structural topology optimization: A review." Structural and Multidisciplinary Optimization, 48(3), pp. 437–472.
[12] Sigmund, O., and Maute, K. (2013). "Topology optimization approaches: A comparative review." Structural and Multidisciplinary Optimization, 48(6), pp. 1031–1055.
[13] Deaton, J. D., and Grandhi, R. V. (2014). "A survey of structural and multidisciplinary continuum topology optimization: Post 2000." Structural and interdisciplinary Optimization, 49(1), pp. 1–38.
[14] Fuchi, K., Ware, T. H., Buskohl, P. R., Reich, G. W., Vaia, R. A., White, T. J., and Joo, J. J., 2015. "Topology optimization for the design of folding liquid crystal elastomer actuators." Soft Matter, 11(37), pp. 7288–7295.
[15] Kwok, T.-H., Wang, C. C. L., Deng, D., Zhang, Y., and Chen, Y. (2015). Journal of Mechanical Design, 137(11), p. 111413. "Four-Dimensional Printing for Freeform Surfaces: Design Optimization of Origami and Kirigami Structures."
[16] Xue, R., Li, R., Du, Z., Zhang, W., Zhu, Y., Sun, Z., and Guo, X. (2017). Extreme Mechanics Letters, 15, pp. 139–144. "Kirigami pattern design of mechanically driven formation of complex 3D structures through topology optimization."
[17] Guo, X., Zhong, W., and Zhang, W. (2014). Journal of Applied Mechanics, 81(8), p. 081009. "Doing Topology Optimization Explicitly and Geometrically A New Moving Morphable Components Based Framework."

[18] Holzapfel, G. (2000). First edition of Nonlinear Solid Mechanics: A Continuum Approach for Engineering, Kluwer Academic Publishers.
[19] Villanueva, C. H., and Maute, K. (2014). "Density and level set-XFEM schemes for topology optimization of 3-D structures." Computational Mechanics, 54(1), pp. 133–150.
[20] Maute, K., and Lawry, M. (2018). "Level set shape and topology optimization of bilateral contact problems with finite strain."
113(8), pp. 1340–1369, International Journal for Numerical Methods in Engineering.
[21] Villanueva, C. H., and Maute, K. (2017). "CutFEM topology optimization of 3D laminar incompressible flow problems."
444–473 in Computer Methods in Applied Mechanics and Engineering, 320 (Supplement C).
[22] Jenkins, N., and Maute, K. (2015). "Level set topology optimization of stationary fluid-structure interaction problems."
52(1), pp. 179–195, Structural and Multidisciplinary Optimization.
[23] Makhija, D., and Maute, K. (2014). "Numerical instabilities in the extended finite element method for level set topology optimization." 185–197 in Structural and Multidisciplinary Optimization, 49(2).
[24] Kreissl, S., and Maute, K. (2012). "Levelset based fluid topology optimization using the extended finite element method." Structural and Multidisciplinary Optimization, 46(3), pp. 311–326.
[25] "A topological derivative method for topology optimization" by Norato, J. A., Bendsøe, M. P., Haber, R. B., and Tortorelli, D. A. (2007). 375–386 in Structural and Multidisciplinary Optimization, 33(4-5).
[26] Bendsøe, M. P. "Optimal shape design as a material distribution problem," 1989. 193–202 in Structural Optimization, 1(4).
[27] "Length scale and manufacturability in density-based topology optimization" by Lazarov, B. S., Wang, F., and Sigmund, O. (2016). 189–218 in Archive of Applied Mechanics, 86(1-2).
[28] Fries, T. P., and Belytschko, T. (2010). "The extended/generalized finite element method: An overview of the method and its applications." International Journal for Numerical Methods in Engineering, 84(3), pp. 253–304.
[29] Hansbo, A., and Hansbo, P. (2004). Computer Methods in Applied Mechanics and Engineering, 193(33–35), pp. 3523–3540. "A finite element method for the simulation of strong and weak discontinuities in solid mechanics."
[30] Terada, K., Yamagishi, M., and Asai, M. (2003). "Linear and non-linear analyses of heterogeneous solids using the finite cover method." International Journal for Numerical Methods in Engineering, 58(9), pp. 1321–1346.
[31] Tran, A. B., Yvonnet, J., He, Q. C., Toulemonde, C., and Sanahuja, J. (2011). "A multiple level set approach to avoid numerical artifacts in XFEM's complex microstructures with adjacent inclusions." 85(11), pp. 1436–1459, International Journal for Numerical Methods in Engineering.
[32] Lang, C., Doostan, A., Makhija, D., and Maute, K. (2014). Computational Mechanics, 54(5), pp. 1357–1374. "A straightforward and effective preconditioning scheme for heaviside enriched XFEM."
[33] Nitsche, J. A. (1971). "A Variationsprinzip zur Losen Dirichlet-Problem bei Verwendung von Teilraum, die ihre Randbedingungen unteworfen sind." Abh. Math. Sem. Univ. Hamburg, 36, pp. 9–15.
[34] "Topology Optimization of Active Structures using a Higher-Order Level-Set-XFEM-Density Approach" by Geiss, M. J., and Maute, K. (2018). 2018 American Institute of Aeronautics and Astronautics Multidisciplinary Analysis and Optimization Conference.
[35] Arora, J. S., and Wang, Q. (2005) "Review of formulations for structural and mechanical system optimization." Structural and Multidisciplinary Optimization, 30(4), pp. 251–272.
[36] Kemmler, R. (2004). "Huge Changes and Stability in the Topology- and Formoptimierung." PhD thesis, University of Stuttgart, p. 187.
[37] Gea, H. C., and Luo, J. (2001). "Topology optimization of structures with geometrical nonlinearities." Computers and Structures, 79(20–21), pp. 1977–1985.
[38] Kreissl, S., Pingen, G., and Maute, K. (2011). "An explicit level set approach for generalized shape optimization of fluids with the lattice Boltzmann method." 496–519 in the International Journal for Numerical Methods in Fluids, 65(5).
[39] Sharma, A., Villanueva, H., and Maute, K. (2017). "On shape sensitivities using heaviside-enriched